

Fluorescence Imaging of Individual Ions and Molecules in Pressurized Noble Gases for Barium Tagging in ^{136}Xe

N. Byrnes,¹ E. Dey,¹ F.W. Foss,² B.J.P. Jones,¹ R. Madigan,² A. McDonald,¹ R.L. Miller,² L.R. Norman,¹ K.E. Navarro,¹ D.R. Nygren,¹ C. Adams,³ H. Almazán,⁴ V. Álvarez,⁵ B. Aparicio,⁶ A.I. Aranburu,⁷ L. Arazi,⁸ I.J. Arnquist,⁹ F. Auria-Luna,⁶ S. Ayet,¹⁰ C.D.R. Azevedo,¹¹ J.E. Barcelon,^{12,7} K. Bailey,³ F. Ballester,⁵ M. del Barrio-Torregrosa,⁷ A. Bayo,¹³ J.M. Benlloch-Rodríguez,⁷ F.I.G.M. Borges,¹⁴ A. Brodolin,^{7,12} S. Cárcel,¹⁰ A. Castillo,⁷ S. Cebrián,¹⁵ E. Church,⁹ L. Cid,¹³ C.A.N. Conde,¹⁴ T. Contreras,¹⁶ F.P. Cossío,^{7,17} G. Díaz,¹⁸ T. Dickel,¹⁹ C. Echevarria,⁷ M. Elorza,⁷ J. Escada,¹⁴ R. Esteve,⁵ R. Felkai,⁸ L.M.P. Fernandes,²⁰ P. Ferrario,^{7,21} A.L. Ferreira,¹¹ Z. Freixa,^{17,21} J. García-Barrena,⁵ J.J. Gómez-Cadenas,^{7,21} R. González,⁷ J.W.R. Grocott,⁴ R. Guenette,⁴ J. Hauptman,²² C.A.O. Henriques,²⁰ J.A. Hernando Morata,¹⁸ P. Herrero-Gómez,²³ V. Herrero,⁵ C. Hervés Carrete,¹⁸ P. Ho,² Y. Ifergan,⁸ F. Kellerer,¹⁰ L. Larizgoitia,⁷ A. Larumbe,⁶ P. Lebrun,²⁴ F. Lopez,⁷ N. López-March,¹⁰ R.D.P. Mano,²⁰ A.P. Marques,¹⁴ J. Martín-Albo,¹⁰ G. Martínez-Lema,⁸ M. Martínez-Vara,⁷ K. Mistry,¹ J. Molina-Canteras,⁶ F. Monrabal,^{7,21} C.M.B. Monteiro,²⁰ F.J. Mora,⁵ P. Novella,¹⁰ A. Nuñez,¹³ E. Oblak,⁷ J. Palacio,¹³ B. Palmeiro,⁴ A. Para,²⁴ I. Parmaksiz,¹ A. Pazos,¹⁷ J. Pelegrin,⁷ M. Pérez Maneiro,¹⁸ M. Querol,¹⁰ A.B. Redwine,⁸ J. Renner,¹⁸ I. Rivilla,^{7,21} C. Rogero,¹² L. Rogers,³ B. Romeo,⁷ C. Romo-Luque,¹⁰ F.P. Santos,¹⁴ J.M.F. dos Santos,²⁰ M. Seemann,⁷ I. Shomroni,²³ P.A.O.C. Silva,²⁰ A. Simón,⁷ S.R. Soleti,⁷ M. Sorel,¹⁰ J. Soto-Oton,¹⁰ J.M.R. Teixeira,²⁰ S. Teruel-Pardo,¹⁰ J.F. Toledo,⁵ C. Tonnelé,⁷ J. Torrent,^{7,25} A. Trettin,⁴ A. Usón,¹⁰ P.R.G. Valle,^{7,17} J.F.C.A. Veloso,¹¹ J. Waiton,⁴ and A. Yubero-Navarro⁷

¹*Department of Physics, University of Texas at Arlington, Arlington, TX 76019, USA*

²*Department of Chemistry and Biochemistry, University of Texas at Arlington, Arlington, TX 76019, USA*

³*Argonne National Laboratory, Argonne, IL 60439, USA*

⁴*Department of Physics and Astronomy, Manchester University, Manchester. M13 9PL, United Kingdom*

⁵*Instituto de Instrumentación para Imagen Molecular (I3M),*

Centro Mixto CSIC - Universitat Politècnica de València, Camino de Vera s/n, Valencia, E-46022, Spain

⁶*Department of Organic Chemistry I, University of the Basque Country (UPV/EHU),*

Centro de Innovación en Química Avanzada (ORFEO-CINQA), San Sebastián / Donostia, E-20018, Spain

⁷*Donostia International Physics Center, BERC Basque Excellence Research Centre,*

Manuel de Lardizabal 4, San Sebastián / Donostia, E-20018, Spain

⁸*Unit of Nuclear Engineering, Faculty of Engineering Sciences,*

Ben-Gurion University of the Negev, P.O.B. 653, Beer-Sheva, 8410501, Israel

⁹*Pacific Northwest National Laboratory (PNNL), Richland, WA 99352, USA*

¹⁰*Instituto de Física Corpuscular (IFIC), CSIC & Universitat de València,*

Calle Catedrático José Beltrán, 2, Paterna, E-46980, Spain

¹¹*Institute of Nanostructures, Nanomodelling and Nanofabrication (i3N),*

Universidade de Aveiro, Campus de Santiago, Aveiro, 3810-193, Portugal

¹²*Centro de Física de Materiales (CFM), CSIC & Universidad del País Vasco (UPV/EHU),
Manuel de Lardizabal 5, San Sebastián / Donostia, E-20018, Spain*

¹³*Laboratorio Subterráneo de Canfranc, Paseo de los Ayerbe s/n, Canfranc Estación, E-22880, Spain*

¹⁴*LIP, Department of Physics, University of Coimbra, Coimbra, 3004-516, Portugal*

¹⁵*Centro de Astropartículas y Física de Altas Energías (CAPA),
Universidad de Zaragoza, Calle Pedro Cerbuna, 12, Zaragoza, E-50009, Spain*

¹⁶*Department of Physics, Harvard University, Cambridge, MA 02138, USA*

¹⁷*Department of Applied Chemistry, Universidad del País Vasco (UPV/EHU),
Manuel de Lardizabal 3, San Sebastián / Donostia, E-20018, Spain*

¹⁸*Instituto Gallego de Física de Altas Energías, Univ. de Santiago de Compostela,
Campus sur, Rúa Xosé María Suárez Núñez, s/n, Santiago de Compostela, E-15782, Spain*

¹⁹*II. Physikalisches Institut, Justus-Liebig-Universität Giessen, Giessen, Germany*

²⁰*LIBPhys, Physics Department, University of Coimbra, Rua Larga, Coimbra, 3004-516, Portugal*

²¹*Ikerbasque (Basque Foundation for Science), Bilbao, E-48009, Spain*

²²*Department of Physics and Astronomy, Iowa State University, Ames, IA 50011-3160, USA*

²³*Racah Institute of Physics, The Hebrew University of Jerusalem, Jerusalem 9190401, Israel*

²⁴*Fermi National Accelerator Laboratory, Batavia, IL 60510, USA*

²⁵*Escola Politècnica Superior, Universitat de Girona, Av. Montilivi, s/n, Girona, E-17071, Spain*

The imaging of individual Ba^{2+} ions in high pressure xenon gas is one possible way to attain background-free sensitivity to neutrinoless double beta decay and hence establish the Majorana nature of the neutrino. In this paper we demonstrate selective single Ba^{2+} ion imaging inside a high-pressure xenon gas environment. Ba^{2+} ions chelated with molecular chemosensors are resolved at the gas-solid interface using a diffraction-limited imaging system with scan area of $1 \times 1 \text{ cm}^2$ located inside 10 bar of xenon gas. This new form of microscopy represents an important enabling step in the development of barium tagging for neutrinoless double beta decay searches in ^{136}Xe , as well as a new tool for studying the photophysics of fluorescent molecules and chemosensors at the solid-gas interface.

The only known sensitive way to establish the Majorana nature of the neutrino is via direct observation of neutrinoless double beta decay ($0\nu\beta\beta$). Its detection would provide a revolutionary insight into the nature of neutrino mass, likely the only observed manifestation of physics above the electroweak scale. It would also be compelling as a potential window into the mechanism leading to the dominance of matter over antimatter in the Universe [1].

All existing techniques to search for $0\nu\beta\beta$ have been limited by backgrounds from radiogenic activity in detector materials [2]. To achieve sensitivity sufficient to discover $0\nu\beta\beta$ if the neutrino mass ordering is inverted and a light Majorana mediates the decay, detectors with ≥ 1 Ton of the double beta decay isotope and background indices of order $b < 0.1(\text{ct ton ROI})^{-1}$ are required [3]. Factors between 20 and 2000 beyond existing demonstrated technologies are required to meet these goals for the immediately forthcoming generation of experiments. Beyond this “ton-scale”

phase [4–7], the task of extending sensitivities into the normal mass ordering band of parameter space appear truly formidable. The relevant experiments would employ far larger quantities of active isotope [8] and require background indices below the ton-scale demands. A distinct but related question is how to confirm a signal of $0\nu\beta\beta$ following a suggestive but inconclusive hint from the coming generation of still-background-limited experiments. New and possibly radically new ultra-low background technologies will be required to meet these challenges.

One especially promising technical approach to reaching the ultra-low background limit is “barium tagging”—identification of the daughter ion produced in the double beta decay of ^{136}Xe [9]. An efficient barium ion tag with low background could reduce contamination from radiogenic backgrounds to near zero. Demonstration of a method of capture and imaging of barium ions from one to several tons of xenon requires significant advances in instrumentation. Much progress has been made on promising methods for single barium ion or atom identification in liquid and gaseous xenon [10–22], but many technological challenges remain.

Most approaches to barium tagging apply some form of fluorescence imaging, exciting transitions in either atoms, molecules, or materials that are caused by presence of a barium atom or ion. In xenon gas experiments, the target charge state for barium tagging is the dication Ba^{2+} , due to absence of recombination from thermalized electrons around the decay [23]. This ion has no low-lying atomic fluorescence lines to access with visible lasers. However, when chelated within a suitable organic molecule, its appearance can in principle be observed via single molecule fluorescence imaging (SMFI). The proposal to use SMFI to tag the daughter ion in $0\nu\beta\beta$ was first outlined in Refs. [17, 24]. Commercial dyes developed for Ca^{2+} sensing in biological applications were demonstrated as sensitive barium tagging agents in solution phase. Soon thereafter, single ion sensitivity was achieved [15]. The model system in that work, liquid droplets within a polymer matrix, is not well representative of conditions within a xenon gas time projection chamber. Several aspects of the chemistry of binding and fluorescence of the commercial dyes were found to be inadequate for dry barium sensing, instigating a program of novel organic fluorophore development, which has culminated in multiple candidates for single Ba^{2+} sensing based on crown-ether derivatives [16, 19, 22, 25–28]. These molecules have been used to demonstrate single molecule sensitivity to barium in dry and solvent-less conditions [18, 28] and shown via electron microscopy to react with neutral barium perchlorate in vacuum [22]. An active ongoing R&D program is underway within the NEXT collaboration to bring these techniques to fruition in barium tagging sensors for a future ton- to multi-ton neutrinoless double beta decay experiment.

Experiments searching for $0\nu\beta\beta$ in ^{136}Xe typically employ time projection chambers filled with purified, pressurized or liquified xenon at part-per-billion purity in oxygen and water to avoid electron attachment. To augment such a detector with a barium tagging system, two distinct problems must be overcome: first, how to bring the ion to a sensor [20, 21] or sensor to an ion [29]; and second, how to sense the arrival of Ba^{2+} with single-ion precision within a large, pure volume of xenon. This is a complex environment in which to realize single ion microscopy, with no commercial devices or past proofs-of-principle available.

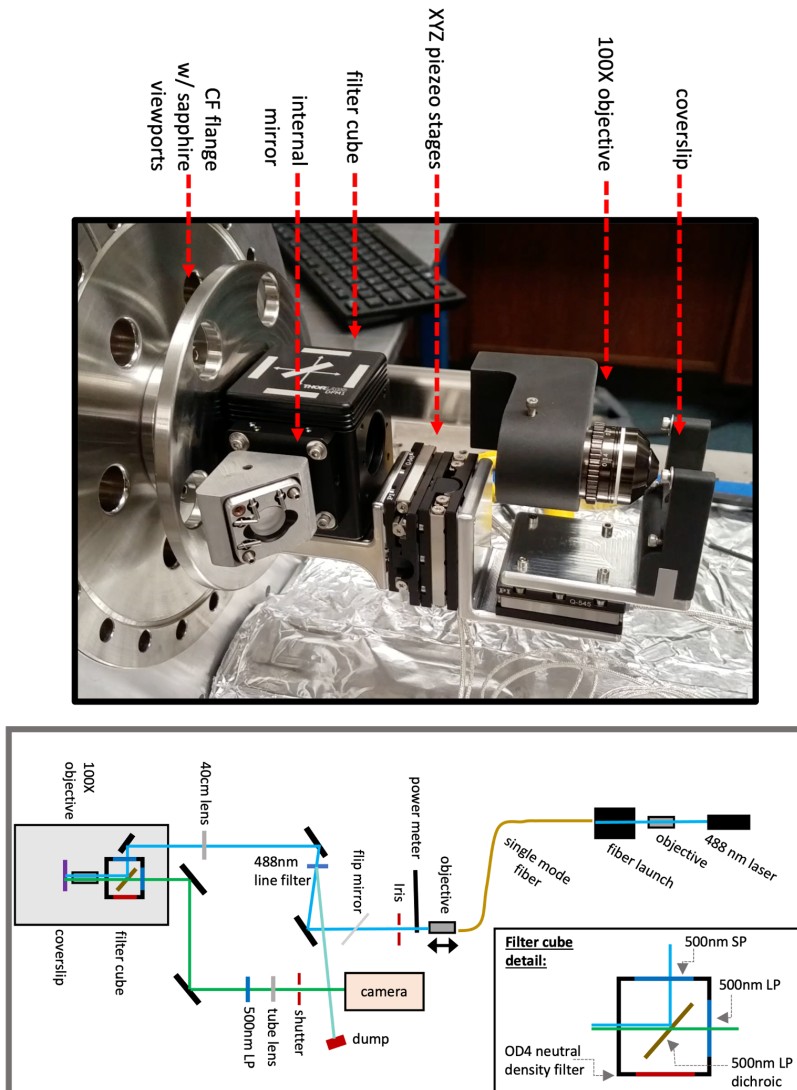


FIG. 1. Top: the head of the high pressure microscope that sits inside the pressure chamber. Bottom: Optical paths and components in the high pressure single molecule microscope.

I. FLUORESCENCE IMAGING OF SINGLE IONS IN HIGH PRESSURE XENON

We present here novel results from NEXT barium tagging program that show a sensing scheme meeting many of the requirements of single ion detection for barium tagging in ^{136}Xe gas. In addition to this motivating application, this technology also opens a new field of single molecule / single ion imaging at the gas-solid interface.

A detailed description of the instrument is provided in the Supplementary Information. Briefly, a fluorescence microscope based on nanometer precision vacuum stages is mounted on the inside of a high pressure chamber connected to a recirculating xenon gas system. Images are recorded by an electron multiplying CCD camera, following laser excitation of barium-induced fluorescence in Ba^{2+} selective organic chemosensors. The system has been characterized using emission from BODIPY fluorophores [30] excited at 488 nm. The configuration for this characterization study

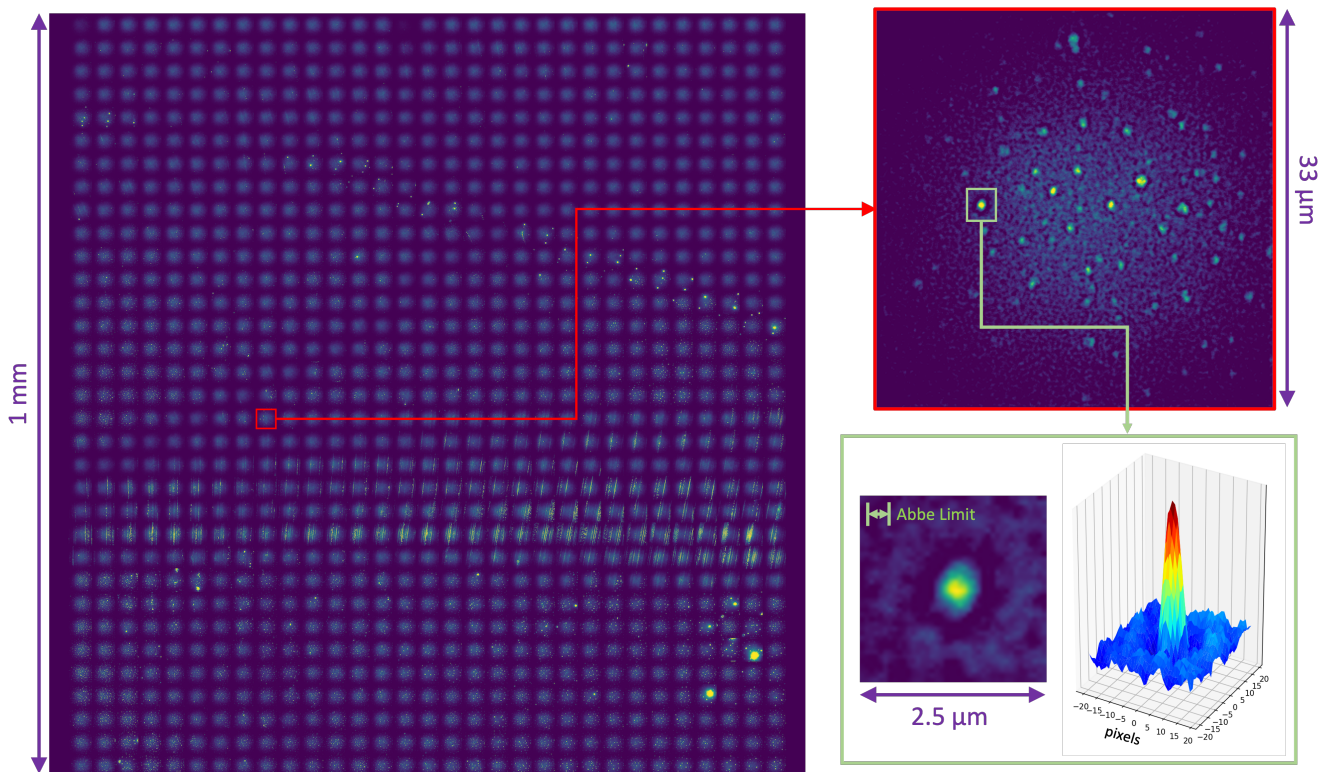


FIG. 2. Large scale raw data image of BODIPY molecules drip-coated onto a slide surface. The image is resolved with point-spread function close to the Abbe Diffraction Limit. Bright points consistent with single molecule fluorescence are observed over a scan region of 1 mm^2 .

is shown in Fig. 1. A raw data image of sparsely distributed molecules, produced by rastering in $33 \mu\text{m}$ steps over a 1 mm^2 surface area and auto-focusing on the single molecule candidates at each point is shown in Fig. 2. The capability for single molecule imaging over this large surface area is clearly demonstrated, with resolution near the Abbe diffraction limit. Further studies of the system imaging resolution can be found in the SI.

To demonstrate single Ba^{2+} ion imaging in high pressure gas, slides were coated with nanomolar concentrations of IPG-1 fluorophore reported in Ref [28]. Solutions were prepared at 10^{-8}M concentration, with and without barium ions supplied via 100 mM barium perchlorate, and activity compared between Ba^{2+} chelated and unchelated samples. The optical system for this test was configured with a 510 nm laser with 10 mW incoming laser power and a filter set suitable for this dye, as described in the SI. The vessel was then sealed, evacuated and filled with cleaned, pressurized xenon. Figure 3 shows images taken under purified 10 bar xenon gas for slides prepared with and without added Ba^{2+} . In this image each frame has been Fourier transformed and spatially filtered. A low pass filter is used to remove the broad background from residual glass fluorescence, and a high pass filter to remove speckles associated with thermal CCD noise. The resultant images display clear bright spots consistent with single molecule emission.

A clear increase in activity is observed upon addition of Ba^{2+} . Some visible streaks in the distribution of single molecule candidates emanate in a radial direction and are a result of the spin-coating protocol. Single molecules remain resolvable within the streaks, though our analysis methods preferentially select those that are isolated single

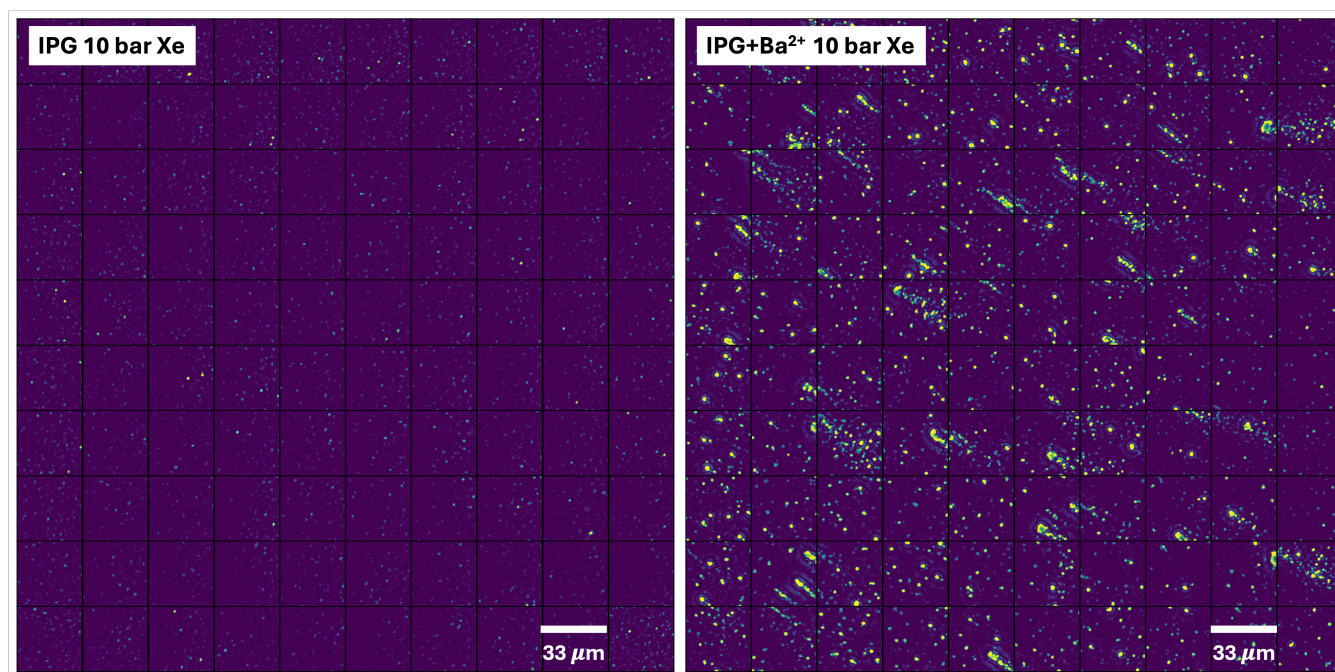


FIG. 3. Image of a slide spin-coated in IPG-1 chemosensor, showing the activity with (right) and without (left) added Ba^{2+} .

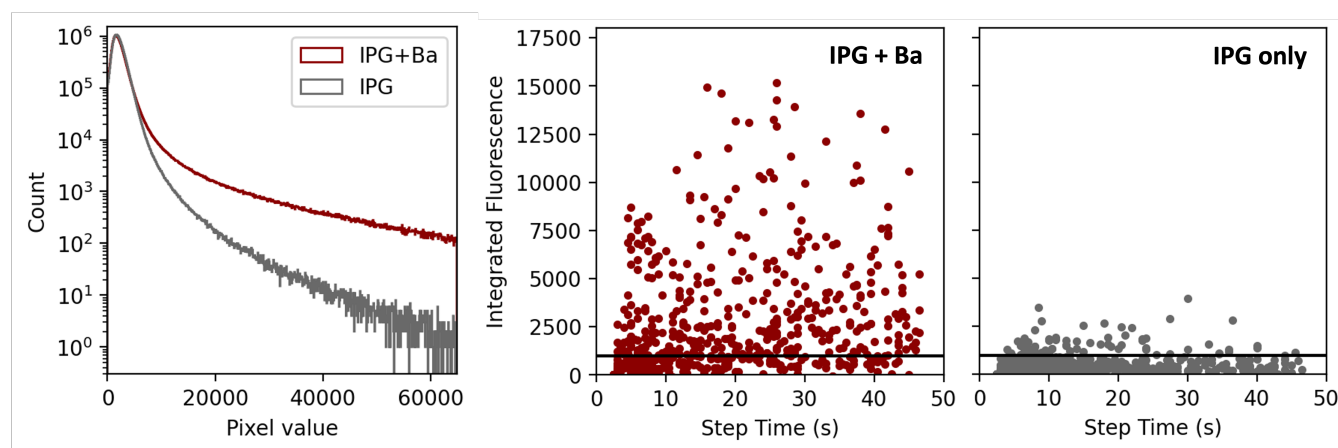


FIG. 4. Left: Pixel intensity distributions for images taken using IPG vs IPG+Ba in 10 bar xenon gas. Right: reconstructed single molecule candidate brightnesses and step times for IPG vs IPG+Ba in 10 bar xenon gas. The plotted points are obtained over seven exposure regions on a single slide, and the trend is found to be repeatable over multiple slides.

spots. The raw pixel histogram indicates a dramatic increase in activity in bright pixels, as shown in, Fig. 4, left. A small number of very weak emitters are present in the Ba^{2+} -free samples, though the bright spots associated with Ba^{2+} -bound IPG molecules are unambiguously identified as being present only in the Ba^{2+} -chelated sample.

As a control experiment, blank coverslips with no fluorophore deposited were also scanned. The characteristic diffuse glow from background fluorescence in the slide was observed in all locations. However, no localized bright emitters could be brought into focus at any point on the slides. This suggests that the background due to accidental fluorescent molecules in the environment is extremely low, and has proven to be unquantifiably so in the present system. Because no emitters could be found, the microscope could not be focused and so no images from the blank

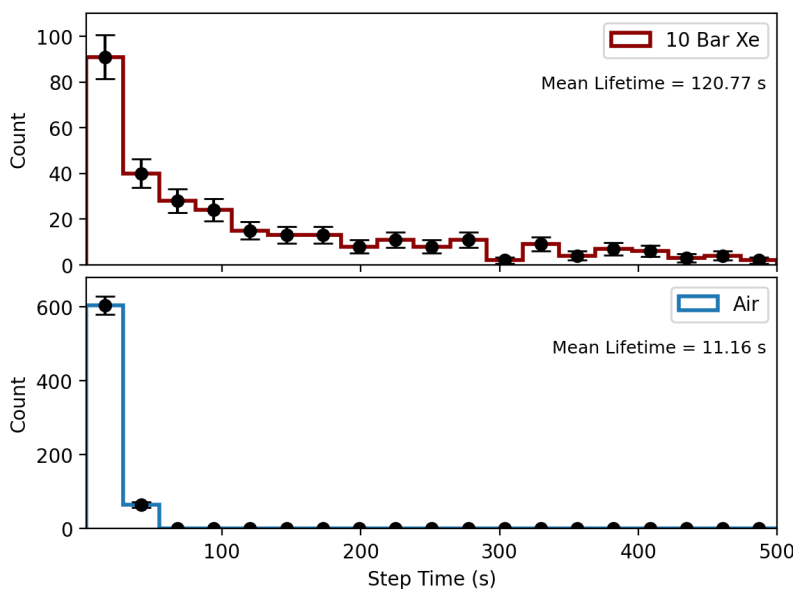


FIG. 5. Photo-bleaching time distribution for Ba^{2+} candidates chelated in IPG dyes in xenon and air. The X axis is shared between the top and bottom histogram.

slide surfaces can be reported.

The hallmark of single molecule fluorescent imaging is bright points that are characterized by their sharp photo-bleaching transitions. A set of analysis tools for single molecule fluorescence imaging and analysis have been developed and are applied to the images captured by the high pressure microscope. To produce a time sequence, the first ten images in a sequence are summed, and a list of local fluorescent maxima ordered by their intensity is used to determine initial points of interest. Each frame is Fourier transformed and convolved with a bipolar filter kernel consisting of one normalized narrow Gaussian (± 4 pixels) with positive amplitude and one normalized broad Gaussian (± 8 pixels) with negative amplitude. This filter serves to subtract local background while integrating fluorescence within the characteristic width of the fluorescent emission area. A cut on the maximal identified step height in each trace is used to identify single molecule photo-bleaching event candidates.

Such candidates are identifiable in all conditions tested, including ambient air, vacuum and and pressurized argon and xenon, in Ba^{2+} spiked samples. The time and intensity distributions of the reconstructed steps in samples with and without Ba^{2+} are provided in Fig. 4, right. In these plots, the y axis corresponds to the fluorescence integral up to the photobleaching transition divided by the total time to the step, providing a measure of average brightness of the emitter. The x axis corresponds to the step time. Only very small steps are observed in the Ba^{2+} -free samples, whereas the Ba^{2+} -enriched ones contain large steps associated with single barium ion candidates.

Fig. 6, left shows the time traces for some single Ba^{2+} ions identified via single-step photo-bleaching 10 bar xenon gas. To the right of each trace are shown the fluorescence intensity maps corresponding to each, representing the activity recorded on a small subset of the CCD pixels. Each surface plot shows the integral of the activity between in the last 20 frames before the photo-bleaching step. The characteristic photo-bleaching and in some cases photoblinking

behaviour associated with single molecule fluorescence imaging is clearly observed in each time series.

Studying the photo-bleaching time distribution illuminates a striking difference in the bleaching dynamics of Ba²⁺-chelated IPG dyes in noble gas vs air environments, with substantially faster bleaching behaviour observed in air. The mean photo-bleaching time in 10 bar xenon gas is extracted as 241.5 s, whereas in air it is much faster at 22.3 s, as shown in Fig. 5. This observation supports the hypothesis that has been discussed in association with solution-based studies (for example, Refs. [31, 32]), that reactions with oxygen are likely primarily responsible for the bleaching process. Nevertheless, even absent ambient oxygen some photo-bleaching mechanism appears to be present, albeit at a far slower rate. While large datasets of IPG+Ba²⁺ images were not collected in vacuum or argon conditions for this work, visual inspection of the photo-bleaching behaviour while imaging in those conditions showed a time profile far more similar to the the xenon data than to air, as may be expected under the oxygen-mediated hypothesis.

II. CONCLUSIONS AND OUTLOOK

We have demonstrated a novel, diffraction-limited, high pressure fluorescence imaging system that is capable of single ion identification in high pressure gases at the gas-solid interface. Single fluorescent molecules are resolved over large surface areas, and we have demonstrated a sweep over $1 \times 1 \text{ mm}^2$ via 2D raster scan. An autofocus algorithm that reliably brings emitters as weak as a single molecule into focus is used to provide a map of the focal plane that can be extrapolated for rapid and repeatable imaging. The total possible scan region is in excess of $1 \times 1 \text{ cm}^2$, with effective focusing possible over the full area.

Single Ba²⁺ ions have been imaged in high pressure xenon gas using turn-on fluorophores, representing the first demonstration of imaging of individual Ba²⁺ ions within a candidate active medium of a time projection chamber for $0\nu\beta\beta$.

The system can be implemented within the pressure vessel of a time projection chamber with only small modifications, which we now briefly discuss. First, in this work, rastering was performed by moving a slide past a fixed objective lens, due to volume limitations within the vessel. In the final device it should be the converse, with rastering of the objective across a fixed imaging region. Since the image rays are brought out of the vessel in infinity space, this will add little in the way of complexity but requires some mechanical adjustments. Second, continuous and lossless operation at this resolution generates a tremendous amount of data (15 GB uncompressed, for the image in Fig. 2). A rational zero suppression algorithm and a form of online trigger for frames of interest is will be advantageous for real-time application, with factors of over 1000 in data reduction to be reasonably expected. These issues require attention, but appear manageable. Finally, the molecular layer used here for Ba²⁺ sensing is produced by spin coating a sparse group of molecules from solution; ultimately a fully sensitive Ba²⁺ tagging layer must use densely packed fluorophores. Detailed investigations into the behaviour of densely packed fluorophore layers on surfaces [22] and into self-assembled monolayer growth [26], as well as studies of the efficiency of barium ion capture at these surfaces using Ba²⁺ ion beams [33] are currently underway within the NEXT collaboration, and represent the next crucial frontier

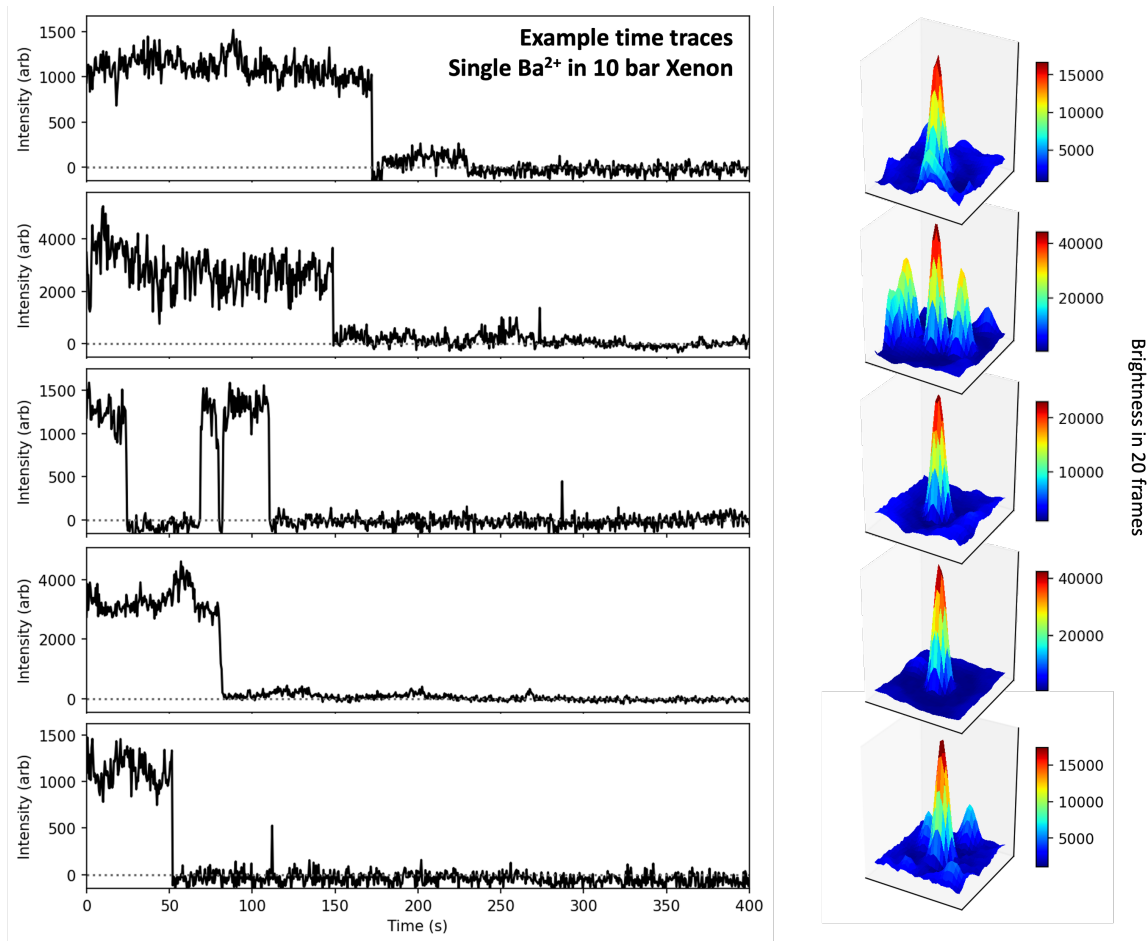


FIG. 6. Single barium ions chelated with IPG-1 turn-on chemosensor imaged in 10 bar xenon gas. The left plots show time traces of fluorescence for the identified emitter, with discrete photobleaching and photoblinking steps indicative of single molecule origin. The intensity is taken from the central pixel after applying a double-Gaussian filter as described in the text, and thus represents the baseline-subtracted integral over the diffraction-limited fluorescent spot. The right figures show the 2D spatial map of fluorescence around each emitter, integrated for 20 frames before photo-bleaching, showing a well localized peak in each case.

in chemical Ba²⁺ ion sensor development. While important work must be done to realize the ultimate sensing layers, an optical system like the one described in this paper will be capable of imaging ions arriving at their surfaces in a future xenon gas barium tagging detector.

Alongside ongoing development of molecular synthesis [16, 19, 22, 25–28], ion transport [21] and detector readout modalities [34–37] that can enable barium tagging at the cathode, the new technology demonstrated in this paper represents an important step toward a large, barium tagging xenon gas detector. Such a device holds great promise as a concept for a truly background free, ton-to-multi-ton scale neutrinoless double beta decay experiment in ¹³⁶Xe. It also represents a first step into a new field of high precision, single molecule photo-physical fluorescence analysis at the gas-solid interface.

ACKNOWLEDGEMENTS

This program of single barium ion sensing is a part of a collaborative project to employ SMFI chemosensors functional at the solid-gas interface, as R&D toward barium tagging for the NEXT experiment. We acknowledge support from the US Department of Energy under awards DE-SC0019054 and DE-SC0019223, and US National Science Foundation under award number NSF CHE 2004111 and the Robert A Welch Foundation under award number Y-2031-20200401 (University of Texas Arlington).

The NEXT Collaboration acknowledges support from the following agencies and institutions: the European Research Council (ERC) under Grant Agreement No. 951281-BOLD; the European Union’s Framework Programme for Research and Innovation Horizon 2020 (2014–2020) under Grant Agreement No. 957202-HIDDEN; the MCIN/AEI of Spain and ERDF A way of making Europe under grants RTI2018-095979 and PID2021-125475NB , the Severo Ochoa Program grant CEX2018-000867-S and the Ramón y Cajal program grant RYC-2015-18820; the Generalitat Valenciana of Spain under grants PROMETEO/2021/087 and CIDEAGENT/2019/049; the Department of Education of the Basque Government of Spain under the predoctoral training program non-doctoral research personnel; the Portuguese FCT under project UID/FIS/04559/2020 to fund the activities of LIBPhys-UC; the Pazy Foundation (Israel) under grants 877040 and 877041; the US Department of Energy under contracts number DE-AC02-06CH11357 (Argonne National Laboratory), DE-AC02-07CH11359 (Fermi National Accelerator Laboratory). Finally, we are grateful to the Laboratorio Subterráneo de Canfranc for hosting and supporting the NEXT experiment.

-
- [1] W. Buchmüller, R. D. Peccei, and T. Yanagida, *Annu. Rev. Nucl. Part. Sci.* **55**, 311 (2005).
 - [2] M. J. Dolinski, A. W. Poon, and W. Rodejohann, *Annual Review of Nuclear and Particle Science* **69**, 219 (2019).
 - [3] M. Agostini, G. Benato, and J. A. Detwiler, *Physical Review D* **96**, 053001 (2017).
 - [4] J. Albert, G. Anton, I. Arnquist, I. Badhrees, P. Barbeau, D. Beck, V. Belov, F. Bourque, J. Brodsky, E. Brown, *et al.*, *Physical Review C* **97**, 065503 (2018).
 - [5] C. Adams, V. Álvarez, L. Arazi, I. Arnquist, C. Azevedo, K. Bailey, F. Ballester, J. Benloch-Rodríguez, F. I. Borges, N. Byrnes, *et al.*, *Journal of High Energy Physics* **2021**, 1 (2021).
 - [6] N. Abgrall, I. Abt, M. Agostini, A. Alexander, C. Andreoiu, G. Araujo, F. Avignone III, W. Bae, A. Bakalyarov, M. Balata, *et al.*, arXiv preprint arXiv:2107.11462 (2021).
 - [7] A. Armatol, C. Augier, F. Avignone III, O. Azzolini, M. Balata, K. Ballen, A. Barabash, G. Bari, A. Barresi, D. Baudin, *et al.*, arXiv preprint arXiv:2203.08386 (2022).
 - [8] A. Avasthi, T. Bowyer, C. Bray, T. Brunner, N. Catarineu, E. Church, R. Guenette, S. Haselschwardt, J. Hayes, M. Heffner, *et al.*, *Physical Review D* **104**, 112007 (2021).
 - [9] M. K. Moe, *Physical Review* **C44**, 931 (1991).
 - [10] C. Chambers *et al.* (nEXO), *Nature* **569**, 203 (2019), arXiv:1806.10694 [physics.ins-det].
 - [11] B. Mong, S. Cook, T. Walton, C. Chambers, A. Craycraft, C. Benitez-Medina, K. Hall, W. F. Jr., J. Albert, D. Auty,

- P. Barbeau, V. Basque, D. Beck, M. Breidenbach, T. Brunner, G. Cao, B. Cleveland, M. Coon, T. Daniels, S. Daugherty, R. DeVoe, T. Didberidze, J. Dilling, M. Dolinski, M. Dunford, L. Fabris, J. Farine, W. Feldmeier, P. Fierlinger, D. Fudenberg, G. Giroux, R. Gornea, K. Graham, G. Gratta, M. Heffner, M. Hughes, X. Jiang, T. Johnson, S. Johnston, A. Karelin, L. Kaufman, R. Killick, T. Koffas, S. Kravitz, R. Krucken, A. Kuchenkov, K. Kumar, D. Leonard, C. Licciardi, Y. Lin, J. Ling, R. MacLellan, M. Marino, D. Moore, A. Odian, I. Ostrovskiy, A. Piepke, A. Pocar, F. Retiere, P. Rowson, M. Roza, A. Schubert, D. Sinclair, E. Smith, V. Stekhanov, M. Tarka, T. Tolba, K. Twelker, J.-L. Vuilleumier, J. Walton, M. Weber, L. Wen, U. Wichoski, L. Yang, Y.-R. Yen, and Y. Zhao, *Physical Review* **A91**, 022505 (2015), arXiv:1410.2624 [physics.atom-ph].
- [12] E. Rollin, *Barium Ion Extraction and Identification from Laser Induced Fluorescence in Gas for the Enriched Xenon Observatory*, Ph.D. thesis, Carleton U. (2011).
- [13] D. Sinclair, E. Rollin, J. Smith, A. Mommers, N. Ackerman, B. Aharmim, M. Auger, P. Barbeau, C. Benitez-Medina, M. Breidenbach, A. Burenkov, S. Cook, A. Coppens, T. Daniels, R. DeVoe, A. Dobi, M. Dolinski, K. Donato, , J. Farine, G. Giroux, G. Gornea, K. Graham, G. Gratta, , C. Hagemann, C. Hall, K. Hall, D. Hallman, C. Hargrove, S. Herrin, L. Kaufman, D. Leonard, F. LePort, D. Mackay, R. MacLennan, B. Mong, M. M. Diez, A. Muller, R. Neilson, E. Niner, A. Odian, K. O’Sullivan, C. Ouellet, A. Piepke, A. Pocar, C. Prescott, K. Pushkin, P. Rowson, S. Slutsky, V. Stekhanov, K. Twelker, N. Voskianian, J. Vuilleumier, U. Wichoski, J. Wodin, L. Yang, and Y. Yen, *Proceedings, 5th Symposium on Large TPCs for Low Energy Rare Event Detection and Workshop on Neutrinos from Supernovae*, *Journal of Physics Conference Series* **309**, 012005 (2011).
- [14] B. Flatt, M. Green, J. Wodin, R. DeVoe, P. Fierlinger, G. Gratta, F. LePort, M. M. Diez, R. Neilson, K. O. A. Pocar, E. Baussan, M. Breidenbach, R. Conley, W. M. Fairbank, Jr., J. Farine, K. Hall, D. Hallman, C. Hargrove, M. Hauger, J. Hodgson, F. Juget, D. Leonard, D. Mackay, Y. Martin, B. Mong, A. Odian, L. Ounalli, A. Piepke, C. Prescott, P. Rowson, K. Skarpaas, D. Schenker, D. Sinclair, V. Strickland, C. Virtue, J.-L. Vuilleumier, J.-M. Vuilleumier, K. Wamba, and P. Weber, *Nuclear Instruments and Methods in Physics Research Section A: Accelerators, Spectrometers, Detectors and Associated Equipment* **A578**, 399 (2007), arXiv:0704.1646 [physics.ins-det].
- [15] A. McDonald, B. Jones, D. Nygren, C. Adams, V. Álvarez, C. Azevedo, J. Benlloch-Rodríguez, F. Borges, A. Botas, S. Cárcel, *et al.*, *Physical review letters* **120**, 132504 (2018).
- [16] I. Rivilla, B. Aparicio, J. M. Bueno, D. Casanova, C. Tonnelé, Z. Freixa, P. Herrero, C. Rogero, J. I. Miranda, R. M. Martínez-Ojeda, *et al.*, *Nature* , 1 (2020).
- [17] B. Jones, A. McDonald, and D. Nygren, *Journal of Instrumentation* **11**, P12011 (2016).
- [18] P. Thapa, N. K. Byrnes, A. A. Denisenko, J. X. Mao, A. D. McDonald, C. A. Newhouse, T. T. Vuong, K. Woodruff, K. Nam, D. R. Nygren, *et al.*, *ACS sensors* **6**, 192 (2021).
- [19] P. Thapa, N. Byrnes, A. Denisenko, F. Foss Jr, B. Jones, J. Mao, K. Nam, C. Newhouse, D. Nygren, A. McDonald, *et al.*, arXiv preprint arXiv:2006.09494 (2020).
- [20] E. Bainglass, B. P. Jones, F. Foss, M. Huda, and D. Nygren, *Phys. Rev. A* **97**, 062509 (2018), arXiv:1804.01169 [physics.ins-det].
- [21] B. Jones, A. Raymond, K. Woodruff, N. Byrnes, A. Denisenko, F. Foss, K. Navarro, D. Nygren, T. Vuong, C. Adams, *et al.*, *Nuclear Instruments and Methods in Physics Research Section A: Accelerators, Spectrometers, Detectors and Associated Equipment* **1039**, 167000 (2022).

- [22] P. Herrero-Gómez, J. Calupitan, M. Ilyn, A. Berdonces-Layunta, T. Wang, D. de Oteyza, M. Corso, R. González-Moreno, I. Rivilla, B. Aparicio, *et al.*, arXiv preprint arXiv:2201.09099 (2022).
- [23] P. Novella, B. Palmeiro, A. Simón, M. Sorel, C. Adams, P. Ferrario, G. Martínez-Lema, F. Monrabal, G. Zuzel, J. J. Gómez-Cadenas, *et al.*, *Journal of High Energy Physics* **2018**, 1 (2018).
- [24] D. R. Nygren, *Nuclear Instruments and Methods in Physics Research Section A: Accelerators, Spectrometers, Detectors and Associated Equipment* **824**, 2 (2016).
- [25] P. Thapa, I. Arnquist, N. Byrnes, A. Denisenko, F. Foss, B. Jones, A. McDonald, D. Nygren, and K. Woodruff, *Scientific reports* **9**, 1 (2019).
- [26] N. K. Byrnes, A. A. Denisenko, F. W. F. Jr., B. J. P. Jones, A. D. McDonald, D. R. Nygren, P. Thapa, and K. Woodruff, arXiv 1909.04677 (2019).
- [27] N. Byrnes, F. Foss Jr, B. Jones, A. McDonald, D. Nygren, P. Thapa, A. Trinidad, N. collaboration, *et al.*, in *Journal of Physics: Conference Series*, Vol. 1312 (IOP Publishing, 2019) p. 012001.
- [28] R. Miller, N. Byrnes, A. Carlson, E. Dey, K. Navarro, R. Madigan, B. Jones, and F. Foss, (2023), <https://doi.org/10.26434/chemrxiv-2023-wxpbh>.
- [29] I. Rivilla *et al.*, arXiv:1909.02782 (2019), arXiv:1909.02782 [physics.ins-det].
- [30] N. Boens, V. Leen, and W. Dehaen, *Chemical Society Reviews* **41**, 1130 (2012).
- [31] Q. Zheng, S. Jockusch, Z. Zhou, and S. C. Blanchard, *Photochemistry and photobiology* **90**, 448 (2014).
- [32] H. Yokota, *Biochimica et Biophysica Acta (BBA)-General Subjects* **1864**, 129362 (2020).
- [33] K. Navarro, J. Baeza-Rubio, M. Boyd, F. Foss, S. Giri, B. Jones, R. Miller, D. Nygren, F. Samaniego, K. Stogsdill, *et al.*, *Journal of Instrumentation* **18**, P07044 (2023).
- [34] S. Soleti, arXiv preprint arXiv:2312.05567 (2023).
- [35] A. Martins, T. Contreras, C. Stanford, M. Tuzi, J. M. Albo, C. O. Escobar, A. Para, A. Kish, J.-S. Park, T. F. Krauss, *et al.*, arXiv preprint arXiv:2401.11315 (2024).
- [36] A. L. Villalpando, J. Martín-Albo, W. Chen, R. Guenette, C. Lego, J. Park, and F. Capasso, *Journal of Instrumentation* **15**, P11021 (2020).
- [37] N. Byrnes, I. Parmaksiz, C. Adams, J. Asaadi, J. Baeza-Rubio, K. Bailey, E. Church, D. González-Díaz, A. Higley, B. Jones, *et al.*, *Journal of Instrumentation* **18**, P08006 (2023).
- [38] Thorlabs P1-405B-FC-2.
- [39] Olympus PLN20X with 0.4 NA.
- [40] Olympus PLN10X.
- [41] Thorlabs FL488-10.
- [42] Thorlabs FEHH0500.
- [43] Thorlabs FELH0500.
- [44] Thorlabs DMLP490R.
- [45] Chroma 49023.
- [46] Customized PLFLN100X; PLAN FLUOR 100X DRY OBJ, NA 0.95, WD 0.2.
- [47] Ted Pella Schott D263M 22x30 mm Glass Coverslips.
- [48] CeramTec 18617-01-CF.

- [49] Thorlabs FELH0500.
- [50] Hamamatsu ImagEM2 EMCCD.
- [51] L. Rogers, R. Clark, B. Jones, A. McDonald, D. Nygren, F. Psihas, C. Adams, V. Álvarez, L. Arazi, C. Azevedo, *et al.*, *Journal of Instrumentation* **13**, P10002 (2018).
- [52] M. Born and E. Wolf, “Principles of optics. sixth (corrected) edition,” (1997).
- [53] PI Q545.140.
- [54] Pfeiffer HiCube 80 Eco.
- [55] Carten HB-51.
- [56] Kurt Lesker KJLC 354.
- [57] SAES PS4-MT3-R-1.
- [58] SAES MicroTorr HP190-902F.
- [59] PumpWorks PW2070.
- [60] Omega FM1800.

III. METHODS

To obtain high quality images, any fluorescence microscope must have carefully arranged optical paths for both illumination and image collection. We begin by describing these optical elements in Sec. III A and III B, respectively, and then describe the mechanical construction of the device in Sec. III D. Section III C describes the alignment and focusing protocol and quantifies some of the imaging metrics of the system.

A. Excitation

Past work on single Ba^{2+} imaging for NEXT has shown that single ion candidates can be observed with at little as 0.2 mW of laser power in the field of view (FOV), corresponding to around 1 W cm^{-2} [15], given molecules with sufficiently high quantum efficiencies. Laser power above a 50 W cm^{-2} , on the other hand, risks rapid photobleaching, preventing the prolonged observation needed to tag a single emitting molecule, for all of the molecular species we have studied. As such we have optimized the current system to provide few-mW levels of excitation to enable clear single molecule resolution, while offering suitably long (few second) observation times to establish presence of an individual ion. We have also opted for an epi-fluorescence configuration. While through-objective total internal reflection fluorescence (TIRF) imaging was used in our earliest studies of fluorescent single barium ion complexes in order to suppress deeper backgrounds arising in thick samples [15], more recent work demonstrated that for sufficiently thin fluorescent samples, single molecule resolution can also be obtained in an epi-fluorescence mode [18]. The latter approach is more straightforward to realize with remote illumination, and forms the basis of our illumination scheme for this device. For this form of microscopy, light is focused on axis on the back-focal plane of the objective by an external lens, leading to parallel and uniform passage of light through the focal plane, which is aligned to the surface supporting the fluorescent emitters to be imaged

We use a series of solid state lasers as excitation sources, each suitable for a different set of fluorescent dyes. For the characterizations of the optical system performance, we have used a 488 nm laser with power controlled by an adjustable DC power supply. This wavelength choice is sufficiently long to escape the tail of fluorescence from glass that compromises single molecule imaging with shorter wavelength excitation (at 450 nm and below, the autofluorescence from the objective and substrate proved prohibitive for single molecule imaging), and is well matched to the absorption peak of the BODIPY [30] molecule used for our optical system characterizations. For Ba^{2+} sensing, a 510 nm laser is used to excite the IPG-1 species studied in Ref. [28]. Due to their long excitation wavelength, the IPG class of molecular probes have been found to provide excellent signal-to-background ratio for single molecule microscopy, in studies undertaken in preparation for this work [28]. An illustrative diagram showing the system configured with the 488 nm laser is shown in Fig. 1, top left.

To obtain smooth excitation profiles over the image plane, the excitation laser beam is first spatially cleaned. For the 488 nm laser, it is first launched from the laser into a single mode optical fiber [38] via a 20X microscope

objective [39]. At the other end of the fiber a 10X objective [40] produces a parallel Gaussian beam of around 2 mm diameter. Longitudinal positioning of this second objective on a micrometer stage allows for fine-tuning of the size of the illumination site on the sensing plane by controlling the beam divergence from the objective. For the 510 nm laser, the beam is instead launched into a 5x beam expander, with adjustable divergence, and then spatially filtered through a pinhole.

Immediately down-beam, a flip-mirror can be used to redirect the laser over a 4 m path to quantify its divergence. Optimal illumination performance was found to correspond to a very slightly divergent beam from this mirror. The excitation light is then passed through an adjustable iris to remove halo. The 488 nm laser configuration then includes a 488 nm laser line filter [41]; whereas for the 510 nm configuration, no subsequent excitation filtering proved to be necessary external to the vessel. The reflected ray from the line filter contains the long and short wavelength tails of the laser spectrum and is absorbed on an external beam dump.

The spatially and spectrally cleaned laser light is reflected from two external adjustable mirrors in a periscope arrangement to allow for fine steering of the path into the vacuum / pressure chamber. The beam next passes through a 1.6 mm thick sapphire pressure window into the vacuum or gas volume. Just in front of the sapphire window, a final 40 cm spherical planoconvex lens is placed at approximately its focal length from the main microscope objective, focusing the nearly parallel beam onto the back-focal plane.

Inside the chamber the beam arrives at a fine-adjustment mirror with two degrees of freedom, which is set before the chamber is closed and left aligned for the duration of the experiment. This mirror directs the beam into an internal filter cube, which has emission and excitation filters and a long-pass dichroic beam splitter. For the 488 nm configuration, these are 500 nm short pass (SP) excitation [42] and 500 nm long pass (LP) emission [43] filters, and a 490 nm dichroic mirror, also LP [44]. For 510 nm, a fluorescence microscopy filter set [45] consisting of excitation filter: band pass 500 ± 20 nm, emission filter: band pass 560 ± 25 nm, and dichroic mirror: long pass 525 nm. On the forth side of the filter cube a high optical density neutral density filter serves as a shallow-depth internal beam dump.

The excitation beam is guided to the back face of a vented 100X, high NA microscope objective [46] which we have customized for operation in high pressure environments. Earlier experiments with commercial objectives resulted in various bursting and internal misalignment failures due to the pressurization and depressurization process. The beam is focused by the objective onto the front face of a 160 μm thick glass coverslip [47] in transmission mode, and the fluorescence emitted from the sample is collected back through the same high numerical aperture objective.

B. Imaging

The longer wavelength fluorescence light emitted from the sample plane transmits through the dichroic mirror and exits through a second 2-inch diameter sapphire viewport [48]. The infinity-space optical path on the fluorescence side is completely enclosed in black optical piping to prevent ambient background from laboratory lighting. The light isolation in the image path is found to be sufficiently effective that single molecule resolution is comfortably

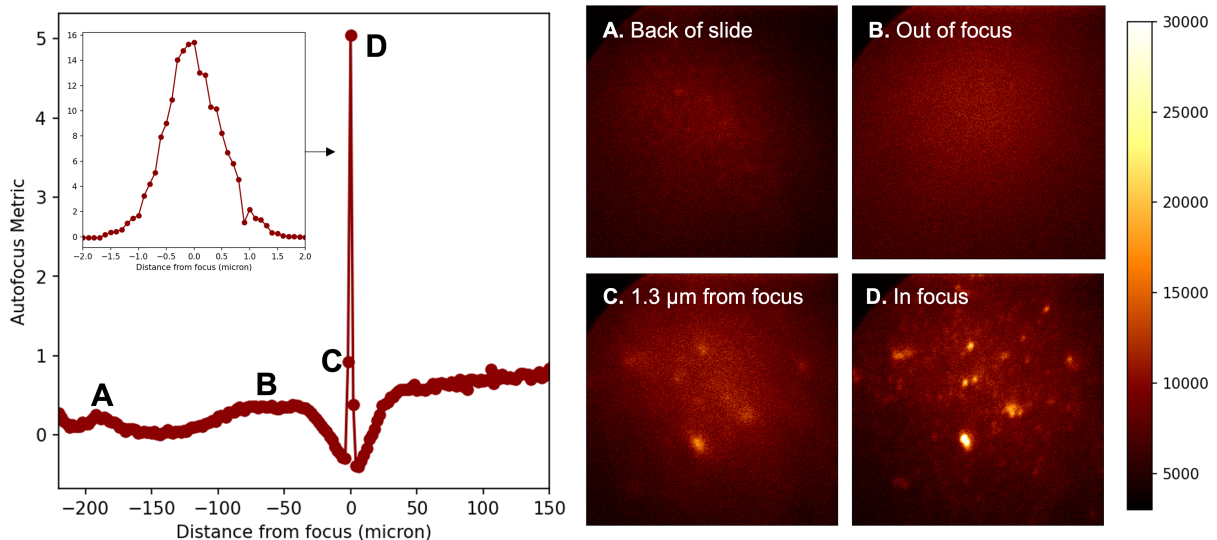


FIG. 7. Illustration of the single molecule autofocus procedure. An autofocus metric defined in terms of image brightness and kurtosis is applied that maximizes for an in focus image. The left plot shows the Z dependence of the autofocus metric, with images at different focal depths provided on the right plot. A small signal is seen on the back face of the slide (A). No features are present when totally out of focus (B). Within around 2 microns of focus some activity is seen (C), with sharp images only at the focal plane (D). The inset shows that the depth of the in-focus region is around $1\mu\text{m}$.

accomplished with laboratory lights on. The image is reflected twice from a pair of mirrors in a periscope arrangement that allow for external adjustment of the region of the objective in the camera FOV. A second, external 500 nm LP filter [49] removes any residual short-wavelength light, and then a tube lens focuses the image from infinity space onto the camera. Adjusting the tube lens position and focal length allows for the system to be run in modes with different levels of magnification. For this paper we have used a medium level of magnification, with approximately $40\mu\text{m}$ field of view per frame achieved using a 15 cm focal length tube lens.

The image acquisition device is an electron multiplying CCD camera [50] with 90% quantum efficiency and a 512×512 array of $16\mu\text{m}\times 16\mu\text{m}$ pixels (pix), operating at 500 ms exposure time. The camera is connected via a demountable tube coupling with an external shutter to protect the camera from being exposed to high light environments. It is read out over IEEE 1394 conduits to a PC running a bespoke data acquisition software suite that we have developed specifically for this device that interfaces to the internal micrometer stages and camera readout.

C. Alignment and Focusing

At each X and Y position there is an approximately $1\mu\text{m}$ deep range of Z values where the fluorescence plane is in focus. Finding this plane at each position requires identification of a weak single molecule fluorescence signal among the range of plausible focal points, which vary by around $70\mu\text{m}$ in absolute terms given repeatability afforded by our slide installation protocol. Few μm variations of the focal plane depth with temperature are observed, consistent with expectations based on thermal expansion of structural materials and the range of temperatures recorded. Furthermore, when changing between gaseous and vacuum conditions we observe a slow drift of the focal plane position on few-hour

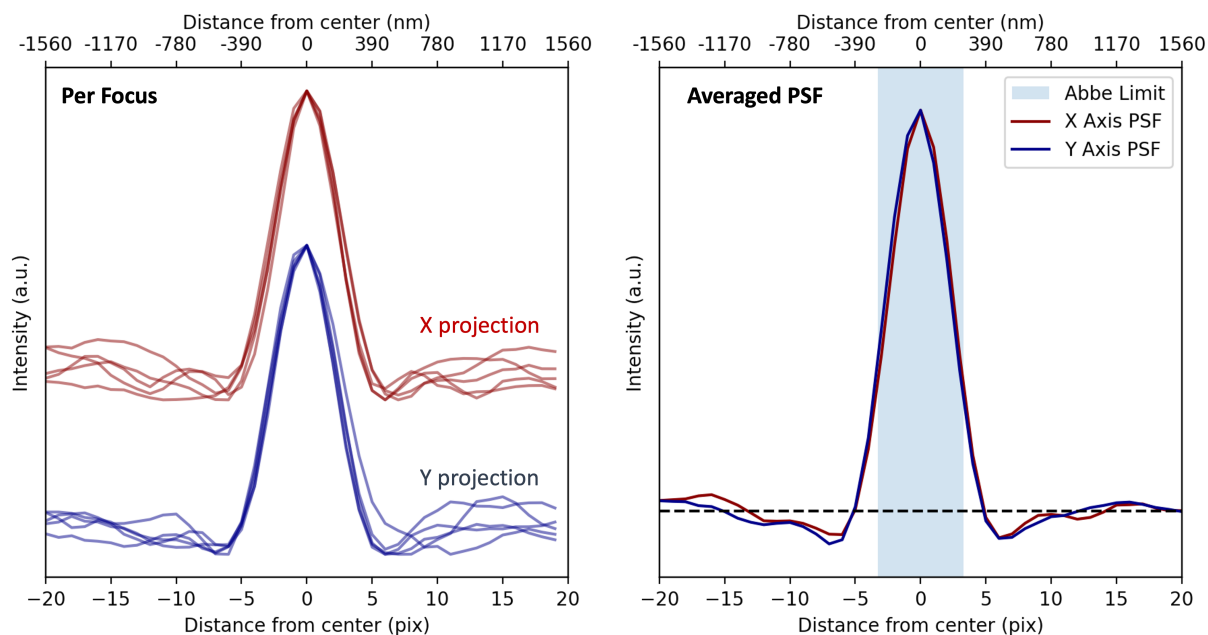


FIG. 8. Left: Measured point-spread function in X and Y directions at five re-focused locations using single molecules in 7 bar argon gas. Right: average X and Y PSF compared to the Abbe diffraction limit. The horizontal line on the right plot represents the baseline, as measured away from the bright spot.

timescales, consistent with the expected effect of swelling of plastics in the structure through gas absorption and degassing [51]. These effects taken together imply that a dynamical method of establishing and tracking the focal plane is required.

To find the focal plane, a single-molecule-sensitive autofocus mechanism has been developed. The focal metric is the ratio of the pixel-wise kurtosis over the mean pixel intensity, which is maximized at each X, Y to establish the focal plane location in stage travel coordinates. This metric favors images with a small number of bright pixels among a field of dimmer ones, which is the characteristic of an in-focus image. Occasionally a cosmic ray muon or radioactive event passes through the EMCCD leading to one or a few extremely bright pixels, presenting to the autofocus metric as an anomalously in-focus image. We exclude such anomalous events by rejecting images with up to 5 bright pixels among a field of otherwise dim ones. This signature can also be distinguished from that associated with an extremely bright fluorescence emitter by its lack of persistence when stationary in the fluorescence plane.

Figure 7 illustrates the performance of the autofocus metric using single BODIPY molecules. Far from the focal plane there are no discernible features, either in the images or in the metric. A set of very dim features are visible on the back of the slide. Since there is no fluorescent layer coated onto this back surface, we interpret these features as being associated with small amount of out-of-focus fluorescence light scattering from optical imperfections on the reverse of the glass. Inside the cover-slip volume no visible features are present. On the far side of the coverslip where we approach the desired focal plane, a sharp spike in autofocus metric is apparent. A higher resolution scan in this region (inset in Fig 7, left) shows that the depth of focus is around $1 \mu m$. Maximizing the autofocus metric is reliably found to obtain focal plane to $\pm 0.3 \mu m$ precision.

After focusing, the images of single point-like emitters exhibit consistent point-spread function (PSF) in air, vacuum and pressurized gases. Fig. 8 shows the X and Y projections of the measured point-spread function obtained using single molecules within 7 bar of argon gas. These PSF projections are obtained by averaging over the the X and Y directions around the brightest 20 fluorescent emitters, re-focusing in 5 distinct locations (Fig. 8, left). The width of the PSF depends slightly upon how perfectly the focal plane has been obtained, but in all cases is very similar to the expectation from Abbe’s theory of diffracting optics [52]. The averaged PSFs in the X and Y directions are compared directly to the Abbe limit in Fig. 8, right. These results suggests that the microscope essentially saturates the theoretical limit of optical resolution, even when running within a pressurized noble gas environment. We note that, due to its single molecule sensitivity, super-resolution techniques can also be used in this system to advance beyond the diffraction limit, though this is of limited value for the barium tagging application.

Once a slide is installed, the standard procedure is to find the focal Z position at 5–10 points on the face of the slide. These data are then used to generate a 3D map of the focal plane by extrapolating a 2D surface through the data points. This fitted focal plane can then be used to find the focus at any other point for subsequent imaging. The focal plane map continues to accumulate data points as in-focus images are found, which serves to continuously refine its precision for extrapolation to new points. This approach allows the focus to be found rapidly at new imaging locations, and thus allows for construction of larger, rastered images by scanning over X - Y positions.

D. Mechanical design and gas handling

The high pressure microscope system is built into a 16 inch long, 6 inch diameter custom-manufactured pressure vessel with 8-inch ConFlat flanges on both ends. The microscope front end-cap is fixed down to an air-levitated optical table with a thick aluminum bracket. Vibration isolation was found to be crucial to achieving optimal resolution, and careful positioning of the various vacuum pumps and circulation pumps around the optical table proved to be instrumental in achieving sharp images. The pressure vessel pipe and back end cap slide on a set of two parallel rails to open and close the vessel, leaving the microscope head fixed in place in order to maintain rough alignment when opening and closing the large CF flanges.

Inside the vessel and cantilevered from the front end-cap, a machined aluminum frame supports a small HDPE bracket that holds the internal microscope objective in a fixed position. A 3-axis vacuum stage system [53] is used to maneuver and monitor a microscope slide in three dimensions in front of the objective. The stage is rated for ultra-high vacuum and has nanometer precision along all three axes, with an active feedback loop inside the device. Our specifications demand only few hundred nanometer precision, below which diffraction limits the point spread function, and the stage comfortably meets these requirements. Careful frequency tuning of the feedback mechanism within the stages had to be made in order to avoid exciting resonant mechanical normal modes of the cantilevered system that inhibited stable positioning. The full range of motion of the stages is ± 6.5 mm in each direction, though our control software restricts the X and Y (in-plane) motion to a region of 10×10 mm and the range of Z (focusing)

motion to within 1.5 mm in front of the microscope slide, to avoid damage from scratching the objective.

The system is evacuated using a turbo pumping station [54] which can be decoupled using an isolation valve [55] when pressurized. Despite the use of some plastics in the system, the vacuum quality as monitored by a hot filament ion gauge [56] routinely reaches 10^{-6} Torr prior to filling with gas, which is an adequate vacuum quality for subsequent fill and operation of time projection chamber detectors. Pressurized xenon gas is supplied to the system by a specially constructed gas handling system. The majority of the gas handling system is formed from 1/4 inch stainless steel piping with Swagelok fittings mounted to a gas control panel. The same system was used to supply purified xenon to the NEXT-CRAB0 detector in Ref. [37].

Noble gases are supplied from cylinders with 99.999% purity and circulated through hot [57] and cold [58] zeolite getters to clean at ~ 3 slpm for several hours to remove oxygen, water and nitrogen contamination. Pumping action is provided by a hermetic, piston-driven gas pump with neoprene buffers [59] with pump-speed controlled by a variac on the power line. Experience with devices on the same gas system show that this is sufficient to achieve part-per-billion levels of oxygen and water impurity. Gas pressure is monitored by several analog pressure gauges on the gas panel and over-pressurization is prevented by a 400 psig relief on the panel, 250 psig relief on the vessel, and a 15 psig burst disk on the vacuum line. The temperature inside the vessel is monitored by an internal thermocouple, and flow both into and out of the vessel in standard liters per minute is monitored using mass flow meters [60].

After running with argon, the gas is typically vented to the room through a vent line, whereas due to its much higher cost xenon is recaptured into bottles by cryogenic condensation with liquid nitrogen. A few psi of xenon is typically lost with each fill cycle due to incompleteness of this capture process. A manifold-like gas mixing arrangement allows for use of multiple gases or mixtures, if needed.